

Lawrence Berkeley National Laboratory

LBL Publications

Title

High-Frequency Light Rectification by Nanoscale Plasmonic Conical Antenna in Point-Contact-Insulator-Metal Architecture

Permalink

<https://escholarship.org/uc/item/0wd6f9bm>

Journal

Advanced Energy Materials, 12(15)

ISSN

1614-6832

Authors

Mupparapu, Rajeshkumar
Cunha, Joao
Tantussi, Francesco
et al.

Publication Date

2022-04-01

DOI

10.1002/aenm.202103785

Copyright Information

This work is made available under the terms of a Creative Commons Attribution License, available at <https://creativecommons.org/licenses/by/4.0/>

Peer reviewed

High-Frequency Light Rectification by Nanoscale Plasmonic Conical Antenna in Point-Contact-Insulator-Metal Architecture

Rajeshkumar Mupparapu, Joao Cunha, Francesco Tantussi, Andrea Jacassi, Leopold Summerer, Maddalena Patrini, Andrea Giugni, Lorenzo Maserati, Alessandro Alabastri,* Denis Garoli, and Remo Proietti Zaccaria*

Numerous efforts have been undertaken to develop rectifying antennas operating at high frequencies, especially dedicated to light harvesting and photo-detection applications. However, the development of efficient high frequency rectifying antennas has been a major technological challenge both due to a lack of comprehension of the underlying physics and limitations in the fabrication techniques. Various rectification strategies have been implemented, including metal-insulator-metal traveling-wave diodes, plasmonic nanogap optical antennas, and whisker diodes, although all show limited high-frequency operation and modest conversion efficiencies. Here a new type of rectifying antenna based on plasmonic carrier generation is demonstrated. The proposed structure consists of a resonant metallic conical nano-antenna tip in contact with the oxide surface of an oxide/metal bilayer. The conical shape allows for an improved current generation based on plasmon-mediated electromagnetic-to-electron conversion, an effect exploiting the nanoscale-tip contact of the rectifying antenna, and proportional to the antenna resonance and to the surface-electron scattering. Importantly, this solution provides rectification operation at 280 THz (1064 nm) with a 100-fold increase in efficiency compared to previously reported results. Finally, the conical rectifying antenna is also demonstrated to operate at 384 THz (780 nm), hence paving a way toward efficient rectennas toward the visible range.

1. Introduction

Direct conversion of electromagnetic radiation into direct current (DC) through a rectification process has been recognized as one of the most appealing strategies for wireless power transmission and detection,^[1] and at the same time, it is considered a viable solution to directly harvest solar energy^[2] as an alternative technology to photovoltaics. By combining a rectifier (i.e., diode) and an antenna, rectenna devices can perform electromagnetic radiation-to-DC conversion.^[3–6] While rectenna devices are known for efficient power conversion in the microwave range, high-frequency rectennas (i.e., at infra-red and visible frequencies) are still far from becoming a practical solution.^[7–10] Even though, efficient rectennas at near-infrared and visible frequencies are very attractive as they could be employed in many scenarios beyond the applications of nowadays photovoltaic

R. Mupparapu, R. Proietti Zaccaria
SPACEiit

Istituto Italiano di Tecnologia
via Morego 30, Genoa 16163, Italy
E-mail: remo.proietti@iit.it


J. Cunha

Integrated Micro and Nanotechnologies
INL - International Iberian Nanotechnology Laboratory
Avenida Mestre José Veiga s/n, Braga 4715-330, Portugal

J. Cunha, L. Summerer
European Space Research and Technology Centre (ESTEC)
European Space Agency

Keplerlaan 1, Noordwijk 2201 AZ, Netherlands

F. Tantussi, A. Jacassi
Plasmon Nanotechnologies
Istituto Italiano di Tecnologia
via Morego 30, Genoa 16163, Italy

 The ORCID identification number(s) for the author(s) of this article can be found under <https://doi.org/10.1002/aenm.202103785>.

© 2022 The Authors. Advanced Energy Materials published by Wiley-VCH GmbH. This is an open access article under the terms of the Creative Commons Attribution-NonCommercial License, which permits use, distribution and reproduction in any medium, provided the original work is properly cited and is not used for commercial purposes.

DOI: 10.1002/aenm.202103785

M. Patrini

Dipartimento di Fisica
Università degli Studi di Pavia
via A. Bassi, 6, Pavia 27100, Italy

A. Giugni

Dipartimento di Fisica
Università degli Studi
LA STATALE
via Celoria 16, Milano 20133, Italy

L. Maserati

Dipartimento di Fisica e Astronomia
Università di Bologna
Viale Berti-Pichat 6/2, Bologna 40127, Italy

A. Alabastri

Department of Electrical and Computer Engineering
Rice University
6100 Main Street, Houston, TX 77005, USA
E-mail: alabastri@rice.edu

D. Garoli

Optoelectronics
Istituto Italiano di Tecnologia
E-mail: via Morego 30, Genoa 16163, Italy

R. Proietti Zaccaria

Ningbo Institute of Materials Technology and Engineering
Chinese Academy of Sciences
Ningbo 315201, China

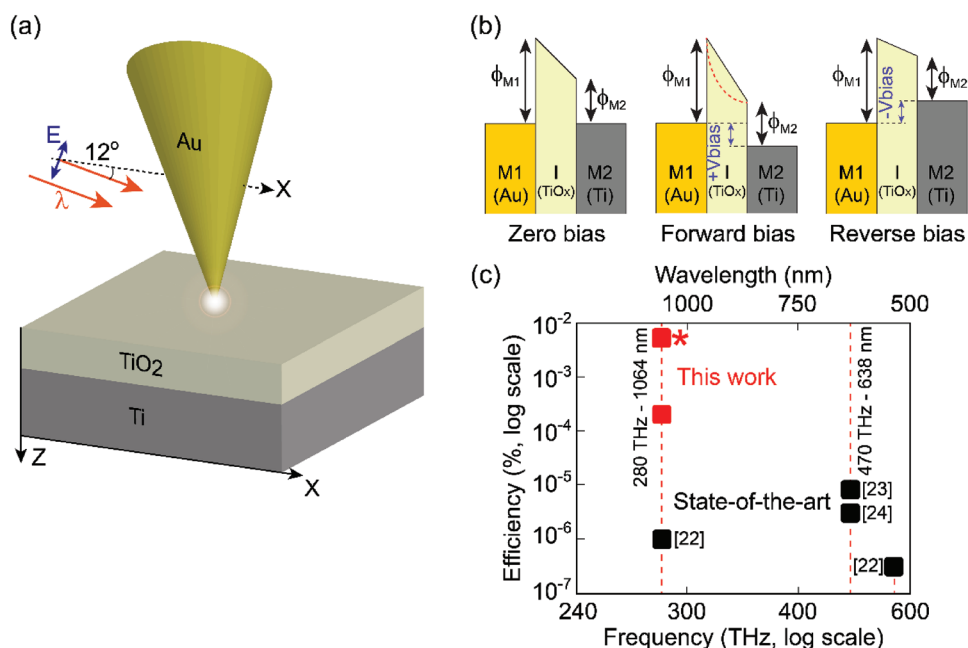


Figure 1. a) Illustration of point contact MIM (pc-M1IM2) nanorectenna illuminated by an externally propagating collimated beam. b) 1D energy diagram of an asymmetric M1IM2 structure. M1 and M2 have work functions ϕ_{M1} and ϕ_{M2} , respectively. Under zero-bias condition, all Fermi levels are aligned. Applying a positive bias to M2 leads to a forward bias situation where electrons near the Fermi level flow from M1 to M2. Applying a negative bias to M2 leads to a reverse bias situation where electrons flow from M2 to M1. The dashed red curve highlighted for the forward bias situation manifests the energy diagram change occurring in point contact configuration. c) Summary of experimental rectennas efficiency at high frequencies. The asterisk (*) refers to an efficiency estimation when only the tip-apex is considered (see Section 2.6).

technology or semiconductor-based photodiodes. For example, high-frequency rectennas could be implemented for power generation at night time or during atmospheric/sand storms by exploiting black body radiation,^[11,12] a solution that could also find an important application in the space sector. Apart from these futuristic and fascinating scenarios, the rectenna concept has been demonstrated in the infrared range^[13–20] also by employing 2D materials,^[20,21] while in the visible range an interesting solution relying on carbon nanotubes (CNTs) was introduced, reaching conversion efficiency up to $\approx 10^{-6}$ %.^[22–24] The limited efficiency values obtained at high-frequencies are attributed to non-optimal geometry of CNTs and fabrication challenges inherent to the bottom-up fabrication process.

Here, aiming to boost the conversion efficiency above the state-of-the-art at near-infrared and toward visible frequencies, we take a different approach, circumventing the previous challenges by exploring nano-antennas engineered through top-down fabrication techniques capable of sustaining plasmonic modes with high-frequency resonances. This choice is motivated by the quest for strong and well localized electric field enhancement, resulting in facilitated electrons extraction when integrated within a rectenna architecture. Following this idea, we have numerically engineered, fabricated, and experimentally characterized a 3D plasmonic nanorectenna operating at 280 THz (1064 nm) and demonstrated the possibility of expanding its operation toward the visible range.

The envisioned architecture and the employed materials were chosen considering that the main aspect of the rectification process is the formation of a preferential current direction, which manifests itself upon the appearance of an

asymmetric current-voltage (I - V) characteristic.^[25,26] To this end, the conceived nanorectenna consists of a fully integrated antenna-rectifier system. Following an asymmetric architecture, both from a geometrical^[27–29] and material^[30] point of view (see Figure 1a and b, respectively), the nanorectenna is defined by a point-contact Metal1-Insulator-Metal2 tunneling diode^[31] (hereafter pc-M1IM2) where the pc-M1 component also plays the role of receiving plasmonic nano-antenna. In particular, we considered an Au-coated nanocone (pc-M1) and a flat 50 nm thick Ti substrate (M2) as the nanorectenna electrodes due to the significant difference in their work functions ϕ ,^[32] with $\phi_{M1} = 5.10$ eV and $\phi_{M2} = 4.33$ eV, respectively (see Figure 1b).

Achieving high-frequency rectification requires nano-scale components. In this respect, Figure 1c depicts the state-of-the-art efficiency of rectennas working at high frequency, from 200 to 600 THz (the red dots represent the results from this work). The plot clearly shows an efficiency decrease upon frequency increase, which strongly highlights the need for nano-scale solutions to improve rectennas efficiency. To this end, we adopted an integrated design to merge the rectifier and antenna functionalities. The fast rectifying component is achieved with a tunneling diode composed of a thin insulator (I) layer coupled to a plasmonic nanocone tip (M1). Indeed, electron tunneling through thin barriers is widely considered to occur at the femto-second scale.^[33,34] Electron tunneling-based devices can thus, in principle, respond to high-frequency radiation (PHz) without lagging. In this perspective, our nanorectenna device employs a few nm-thick TiO_x (I) layer on top of a Ti (M2) electrode, finally resulting in a remarkable efficiency improvement with respect to the state-of-the-art.

From a classical point of view, the maximum achievable rectification frequency ω_{rect} is proportional to the inverse of the of resistance and capacitance associated with the tip/substrate system, which in turn is found to increase upon reduction of the tip-apex dimension.^[35] This result, even though deriving from the classical approximation of the metal-insulator-metal (MIM) described in terms of lumped circuit elements, highlights the importance of a nanometric-sized metallic tip for high-frequency operation. This requirement is further stressed by the reduction of the electron mean free path ($e\text{MFP}$) upon frequency increase ($\approx 1/\omega^2$).^[36] Moreover, a reduced apex size determines an enhancement of surface electron scattering, allowing to expel electrons more efficiently than a planar metallic surface. This physical characteristics represents an added element of asymmetry to the already mentioned geometrical and material asymmetries, all supporting the flow of a DC current from the nanocone tip toward the Ti layer passing through the TiO_x barrier. Additionally, no strong coupling effects between the plasmonic mode and the TiO_x are expected^[37–39] due to the very different frequency positioning of the TiO_x absorption peak (≈ 300 nm) and the plasmonic mode resonance (1064 nm).

Via the scheme of the pc-M1IM2 nanorectenna shown in Figure 1a, electromagnetic radiation is harnessed and converted into surface plasmon resonances (SPRs, with energy $\hbar\omega_{\text{pl}}$ where $\omega_{\text{pl}} = 2\pi c/\lambda_{\text{inc}}$) by the plasmonic nanocone (pc-M1). The conical shape of the antenna supports asymmetric plasmonic modes that favour electromagnetic energy concentration at the apex of the structure.^[40] Moreover, the damping rate of plasmons,

which causes the excitation of electron-hole pairs, shows a conversion rate which scales inversely proportional to the square of the curvature radius,^[41,42] namely related to geometrical constrictions that fosters surface scattering events.^[43,44] This process produces a relatively large concentration of hot-electrons (HEs), with energies up to $\hbar\omega_{\text{pl}}$ above the Fermi level, available for tunneling through the insulator layer. Importantly, surface scattering relaxes the linear momentum conservation constraint facilitating the plasmon-exciton coupling and the emission of electrons along the plasmon propagation direction.^[45] These considerations suggest that HEs can be efficiently generated mainly at the tip-apex, which is coincidentally at the right position for getting collected, being the tip-apex in contact with the TiO_x insulator layer. In this respect, the cone-to-substrate contact radius C_r (≈ 1.3 nm, see Supporting Information) with a dimension much smaller than the electron mean free path in Au (≈ 40 nm^[36]), facilitates the collection through the TiO_x barrier by tunneling mechanism of most of the HEs generated in the gold nanocone.^[46,47]

2. Results and Discussion

2.1. Optical Design and Simulations

To identify a good performing geometrical configuration, we employed both analytical and 3D Finite Element Method (FEM) numerical simulations (see Experimental Section

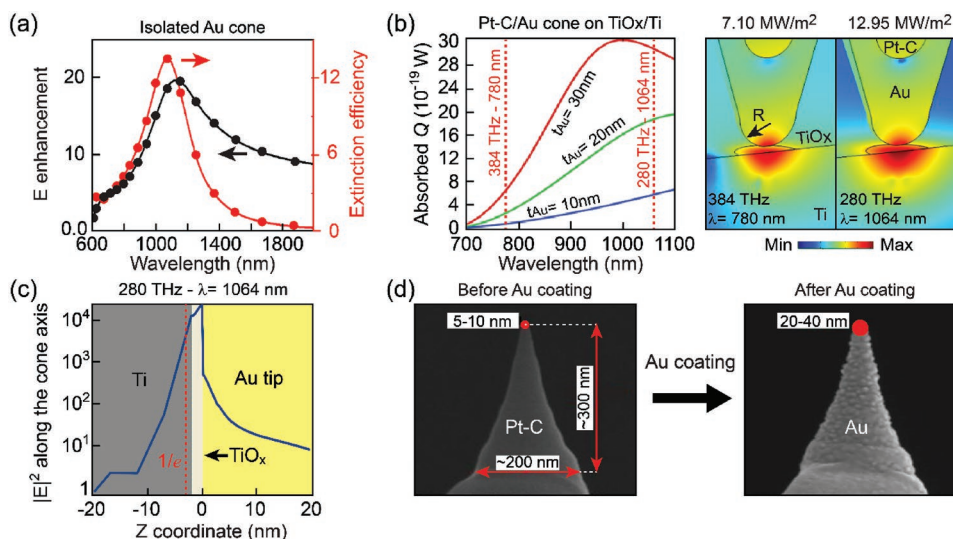


Figure 2. a) Extinction spectrum from an isolated Au nanocone and its electric near-field enhancement factor calculated at the cone apex. Resonance at $\lambda \approx 1064$ nm (280 THz) is found for an Au nanocone with height 300 nm and base diameter 200 nm. The simulated linearly polarized incident radiation is tilted by 12° with respect to the normal of the cone axis (X-axis in Figure 1a), as shown in Figure 1a, mimicking the experimental conditions. b) Absorbed electromagnetic power Q versus wavelength calculated in the apex-end of the Au tip, for three Au coating thicknesses (i.e., 10, 20, and 30 nm, always within the $e\text{MFP}$). The cone is formed by a Pt-C core with base 200 nm, height 300 nm, Pt-C tip radius $R = 20$ nm, and covered with a top-deposited Au layer with thickness $t_{\text{Au}} = 20$ nm (all these values represent the experimental parameters). In the simulations, the experimental evaluation of the contact radius C_r and substrate thickness have been employed as well, with $C_r = 1.3$ nm, $\text{TiO}_x \approx 2$ nm, and $\text{Ti} = 50$ nm (see Supporting Information). In the right, the figure also shows the absorption maps calculated at 780 and 1064 nm for input intensities of 7.10 and 12.95 MW m⁻², respectively. From the scale bar, the strongest absorption is obtained at $\lambda = 1064$ nm. c) $|E|^2$ in logarithmic scale calculated along a line passing through the center of the cone. $Z = 0$ corresponds to the contact point between the Au tip and the TiO_x substrate, $Z > 0$ corresponds to the Au coating of the tip. The dashed line represents the position in the substrate where the electric field has decayed down to $1/e$ of its maximum value. d) SEM image of the nanocone fabricated on the AFM milled probe before (core formed by Pt-C) and after Au coating. The red dots represent the tip radius (different coating thicknesses have been considered returning an overall tip radius in the range 20–40 nm).

and Supporting Information). In particular, the analytical approach^[48] was chosen to gain a quick grasp on the dimensions of an isolated Au nanocone with a resonance around 280 THz (1064 nm) and still be operative at 384 THz (780 nm). The resulting cone dimensions, base diameter 200 nm and height 300 nm, were fed into our FEM numerical model to confirm the resonance frequency both in terms of electric field enhancement (near-field) and extinction (far-field), as shown in **Figure 2a**. Afterward, a full FEM analysis was performed taking into account the contributions from realistic aspects present in the actual experiment such as i) the contact radius, ii) the Pt-C core of the cone (as resulting from the fabrication process), and iii) the presence of the TiO_x/Ti substrate. Additionally, the 3D FEM model was employed to estimate the total electromagnetic power density $Q = \frac{1}{2} \omega \epsilon_0 \text{Im}(\epsilon_r) E^2$ absorbed by the conical tip (the corresponding power, integrated within the apex volume, is shown **Figure 2b**, left), which is a good estimator of the HEs capable of crossing the MIM barrier.^[43] Indeed, three Au coating thicknesses were considered (i.e., 10, 20, 30 nm), all below the ϵ MFP of Au in the visible range. Furthermore, with a ≈ 2 nm-thick TiO_x layer on top of 50 nm of Ti (see Supporting Information), the simulation results show a resonance shift with respect to **Figure 2a**. This result highlights the importance of considering the actual materials involved in the cone fabrication (Au & Pt-C versus Au) together with the substrate when estimating the frequency of the cone resonances. The absorption maps (**Figure 2b**, right) at 280 THz (1064 nm) and 384 THz (780 nm) show an absorption mostly localized at the apex region, reinforcing the consideration that the HEs involved in the photocurrent generation mainly originate from the zone of the cone localized in proximity (i.e., within the ϵ MFP) of the TiO_x substrate. In terms of power absorption at 280 and 384 THz, our numerical results show a better performance for the 280 THz case (later confirmed by a higher 280 THz experimental photocurrent). This result can be qualitatively explained by recalling that i) the nanocone dimensions were chosen to specifically sustain the 280 THz mode, and ii) the ϵ MFP goes with ω^{-2} ,^[36] thus determining a reduced photocurrent upon frequency increase.

Figure 2c shows the electric field intensity calculated along the cone axis into the substrate materials. A quick field intensity decay into the Ti layer ($1/e$ is reached after just 2.3 nm from the TiO_x/Au interface) suggests limited HEs generation into the substrate due to the tip radiated field. It should also be noted that the absolute value of the k -vector associated with photons is generally much smaller than the wave vector associated with free electrons in a metal, thereby strengthening the picture of a negligible photocurrent contribution due to photons directly impinging on the Ti substrate.

2.2. Nanorectenna Fabrication and Characterization

Upon identifying a set of geometrical parameters for an adequate optical performance through numerical calculations, the next step was to fabricate the system formed by the Pt-C/Au nanocone in contact with a TiO_x/Ti substrate. In particular, the nanocone shown in **Figure 2d** was realized on top of an atomic force microscope (AFM) cantilever through focus ion beam

(FIB) lithography (see Experimental Section). The AFM was used to characterize the pc-M1IM2 nanorectenna through precise control over the landing position of the Au nanocone and by tuning its contact force on the TiO_x. This set-up features the AFM scanning contact mode of the nanocone over the substrate surface while detecting, with nanometric resolution, structural defects in the MIM junction (see Experimental Section). Furthermore, the characterization set-up consisted of laser sources, optical components, pico-current amplifier, and electronics to simultaneously perform modulated optical excitation and synchronous electrical detection measurements (see Experimental Section and Supporting Information). In this regard, with the final objective of determining the performance of the proposed nanorectenna architecture, we measured the I - V characteristic of the junction composed of a single Au nanocone brought in contact with TiO_x natively grown on a Ti film (for TiO_x deposited via atomic layer deposition see Supporting Information), which was characterized via XPS and ellipsometry (see Supporting Information). **Figure 3a** shows the experimental I - V nanorectenna characteristics obtained in dark and illuminated conditions, the latter resulting from illuminating the nanocone with a 100% amplitude modulated square wave profile beam with $\approx 4 \mu\text{m}$ wide focal spot. It is evident from the figure that the current measured in the forward bias under dark conditions is quantitatively higher than the reverse bias counterpart, confirming the diode-like (asymmetric) behavior of the nanorectenna. Furthermore, upon illumination, additional current is generated in the pc-M1IM2, as confirmed in **Figure 3b**, where the synchronism between the measured current and the laser modulation is demonstrated. We shall stress that this extra current generation also occurs at 0 voltage, that is, the ideal light-detection condition, as it rules out any possible effect due to the applied bias.

In our nanorectenna device, different physical mechanisms concur in the final result. In this regard, the energy diagram of the pc-M1IM2 nanorectenna shown in **Figure 1b** is a useful tool, although its construction is complex as it depends on both material properties and interfaces geometrical configuration. Specifically, the 3D nature of the point contact geometry^[28] challenges the applicability of the simple 1D energy diagram shown in **Figure 1b**. The actual energy diagram shows pronounced convexity/concavity (see red dashed line under forward bias) due to i) conical geometry of the point contact and ii) image force/electrostatic effects depending on the applied bias condition.^[49] In particular, when pc-M1 and IM2 are brought together to form a junction, the bands will tilt due to the adjustment of the Fermi levels. Under forward bias conditions, the Fermi level of M2 is lowered with a consequent tilting and bending of the band (red dashed line in **Figure 1b**), resulting in a narrowing of the oxide barrier. Especially in our case, where a strong asymmetry characterizes the pc-M1IM2, a small bias can significantly tilt the barrier, thus allowing for an enhanced tunneling current in the top part of the energy diagram (similar considerations apply for reverse bias).

Overall, due to the nanorectenna shape and choice of materials, two main mechanisms can contribute to the current flowing from M1 to M2 in the pc-M1IM2 structure: i) direct tunneling, namely HEs tunneling through the barrier with a width equal to the thickness of the insulator, and ii) Fowler-Nordheim

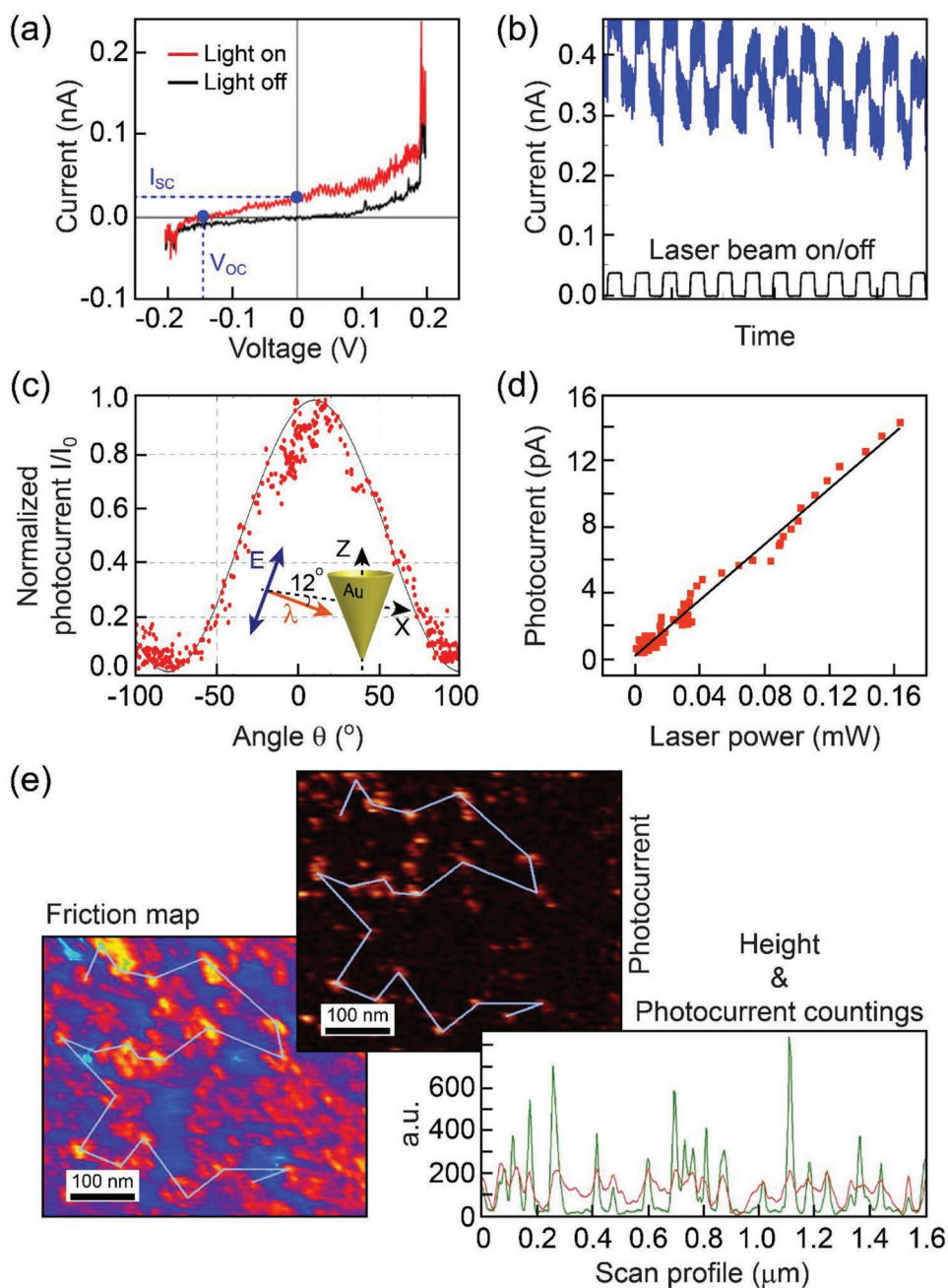


Figure 3. a) I - V characteristic of a single Au nanocone (20 nm Au coating)/TiO_x/Ti-50 nm nanorectenna. The black and red curves denote dark and illuminated current, respectively. The employed wavelength is $\lambda = 1064$ nm with an input intensity equal to 12.95 MW m^{-2} . The short circuit current I_{SC} and the open circuit voltage V_{OC} are highlighted. b) Temporal profiles of the laser beam (black color) and simultaneously measured current (blue color) in the rectenna. The distance between two adjacent peaks in the horizontal axis is ≈ 2.7 ms, corresponding to a modulation frequency of 371 Hz (see Supporting Information). The applied bias varies with time between 0.11 and 0.15 V (see Experimental Section). c) Photocurrent versus polarization angle. d) Photocurrent versus laser power measured by applying a phase lock-in technique (see Supporting Information). e) Friction (topography) map acquired on the substrate (left) and the concurrently acquired photocurrent map (center). The relation between the friction map (red line) and the corresponding photocurrent (green line) is also shown (right). See Supporting Information for details.

(FN) tunneling, where HEs tunnel through the triangular-shaped tilted barrier with a width smaller than the insulator thickness. In particular, we highlight that both the direct and Fowler-Nordheim mechanisms benefit from forming a plasmonic resonance on the nanocone. Indeed, this allows for the

excitation of HEs physically located near the interface M1-I, capable of transitioning from the Au nanocone tip into the TiO_x/Ti substrate. A contending physical mechanism to excitation and transfer of electrons across the nanorectenna is the internal photoemission (IPE). This phenomenon describes the

direct electron-hole pairs excitation (non-plasmon mediated) in the bulk of the M1 metal. By considering the fast electron-electron thermalization (the few nanometers long e MFP in Au), it can be argued that only the IPE excitons generated at the tip apex could contribute to the photocurrent. It can be then concluded that the number of IPE-generated e - h pairs contributing to the total current becomes negligible when considering that it results from the product of the impinging radiation intensity, the quantum coupling efficiency, and the M1-I contact area ($Cr \approx 1.3$ nm).^[50] Furthermore, if the frequency of the incoming electromagnetic radiation is sufficiently high, IPE excitons could also comprise vertical interband transitions, where electrons energetically located at inner energy bands in M1 are brought slightly above the Fermi level, at the expense of most of the absorbed electromagnetic energy (specifically for Au, the transition from d-band to sp-band would require 1.8–2.4 eV \approx 500–700 nm.)^[51] In this case, the promoted electrons barely possess enough energy to go through the insulator barrier, hence limiting the overall current flow.^[52]

Apart from the transport mechanism, we argue that the optical absorption efficiency enhancement of the plasmonic nanocone likely improves the performance of the rectenna, especially in terms of output current, particularly by confining light at the apex region. The experimental confirmation of the resonant nature of the rectification process occurring in the nanorectenna device is provided by the polarization measurements depicted in Figure 3c. The figure shows the $\cos^2\theta$ dependence of the photocurrent, where the value $\theta = 0$ represents the polarization along the Z -axis (see inset). The result demonstrates the maximum outcome for light polarized along the nanocone main axis, namely for a maximum value of the SPR coupling. The two aspects of maximal absorption efficiency and photocurrent for light polarized along the cone axis, bring about two major considerations: i) the cones should be kept sufficiently apart to avoid any reciprocal shadowing effect, a situation which would increase the rectenna device footprint; ii) the sunlight is non polarized therefore part of it would not be captured by the conical antenna. These are two interconnected challenges that need to be addressed when designing future conical rectenna devices, for example by envisioning a non-resonant and polarization-free solution based on specific mode generation.^[40] Figure 3d highlights the dependence of the photo-generated current on the laser power, showing a clear linear dependence. This result agrees with previous works,^[24,49,53,54] and it confirms the main role of tunneling processes in photocurrent generation as described by the photon-assisted tunneling theory (see Section 2.3).

Besides the nanocone dimensions, material composition, and the impinging radiation wavelength responsible for the SPRs formation, the topography of the IM2 also influences the photocurrent amplitude. In this regard, to determine the role of the substrate morphology on the measured photocurrent, we simultaneously mapped the friction and the corresponding photocurrent over a randomly chosen region of TiO_x/Ti-50 nm under gentle mechanical contact condition, as shown in Figure 3e. The correlation between these two quantities is plotted, indicating that the highest photocurrents are recorded on top of the TiO_x/Ti-50 nm grains. This result suggests that

the best performance can be achieved only when the outmost end of the nanocone apex is in contact with the substrate, corresponding to a minimized contact area.^[49] Furthermore, in the Supporting Information we show the photocurrent maps obtained by applying different contact forces to the IM2 nanorectenna component, suggesting a signal decrease with the increase of the contact force (i.e., bigger contact radius). This result highlights the importance of a controlled contact force to maximize the nanorectenna photocurrent.

2.3. Photon-Assisted Tunneling theory

Among the fundamental parameters determining the actual photocurrent generated by the nanorectenna device, we shall recognize the barrier height, barrier thickness, and tunneling area. In this regard, as demonstrated in previous theoretical and experimental studies,^[17,22–24,55] studies, when a tunnel junction is illuminated with radiation of energy $\hbar\omega_{ph}$, an AC voltage of the form $V_{opt} \cdot \cos(\omega_{ph} \cdot t)$ develops across the junction which leads to a net DC current component. This DC component, following Tien-Gordon and Tucker formulation, is described by the time-averaged Photon-Assisted Tunneling (PAT) theory:^[56–58]

$$I_{illum}(V) = \sum_{k=-\infty}^{\infty} J_k^2 \left(\frac{eV_{opt}}{\hbar\omega_{ph}} \right) I_{dark} \left(V + \frac{k\hbar\omega_{ph}}{e} \right) \quad (1)$$

with k referring to the number of quanta exchanged in the electron tunneling process, J_k being the Bessel function of k -th order whose square describes the probability of an electron transition from its initial state to an energy level modified by k -quanta, and V is the applied DC voltage. Under the assumption of $eV_{opt} \ll \hbar\omega_{ph}$ it results to be $k \approx -1, 0, 1$, which simplifies Equation (1) (this assumption is realistic at high incident frequencies ω_{ph} such as the visible range). Furthermore, the characteristic I_{dark} reflects the transport mechanisms in dark conditions (i.e., no light)—direct or Fowler-Nordheim (FN) tunneling—and it depends on the employed materials (M1, I, and M2), their geometry, the voltage applied to the junction and temperature. In particular, the transition voltage^[59] between direct and FN tunneling is estimated by the position of the local minimum (inflection point^[6,52,59]) in the FN representation of the $I_{dark}(V)$ curve.

The experimentally measured I_{dark} depicted in the FN representation of Figure 4a (blue dots) highlights the absence of any inflection points, suggesting direct tunneling as the preferential transport mechanism across the nanorectenna. A fit of the experimental $I_{dark}(V)$ characteristic (Figure 4a, black lines) was then performed by employing the Simmons' model^[60] (see Supporting Information), and it was used to determine the effective parameters of the junction band diagram. We obtained an average effective barrier height of 3.94 eV, an effective barrier thickness of 1.5 nm (in agreement with ellipsometry data, see Supporting Information) and an effective tunneling area of 1 nm². This last value is consistent with small tunneling electrical contacts reported in the literature,^[61] where it is shown that electrical contact area is usually smaller than the mechanical contact area (≈ 5 nm², contact radius of 1.3 nm, see Supporting Information). The parameters obtained from the

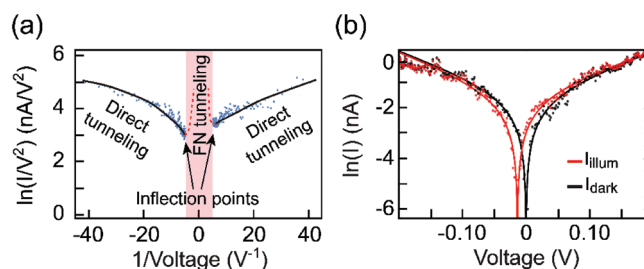


Figure 4. a) Fowler-Nordheim representation of the I - V curve in dark condition. The blue dots are the experimental data. The continuous lines (black color) represent the experimental data fitting describing the occurrence of direct tunneling. The dashed lines (red color) represent the FN tunneling, absent in the present case, as no inflection points are found at the intersection between direct and FN tunneling. b) Simmons' fit (continuous line) of the I - V curves in both dark and illumination conditions (the dots are the experimental data). The fitting has an uncertainty of 10%. The vertical axis describes the natural logarithm of the electric current absolute value.

$I_{\text{dark}}(V)$ fitting were finally employed within the PAT expression (Equation (1)) to calculate the I - V characteristic under illuminated conditions compared with the experimental data. In particular, a V_{opt} equal to 10 mV was used to achieve the theoretical/experimental matching shown in Figure 4b, both under dark and illumination conditions. This result strongly suggests that the PAT theory may indeed be employed to describe the transport mechanisms in pc-M1IM2 nanorectennas. It also agrees with the aforementioned results of Figure 3d on the dependence between laser power intensity and generated power current, where a linear relationship was depicted.^[49,53]

Importantly, it should be pointed out that the Simmons' and PAT models properly apply to traditional MIM systems whereas, in the present case, the geometrical configuration differentiates from them both in terms of asymmetrical geometry and the possible generation of SPRs at the cone side. Hence, particular care should be given in avoiding strict conclusions only by fitting I - V electrical characteristics.^[62] For this reason, the geometrical estimates originating from the aforementioned fitting procedure should be confirmed by independent secondary approaches which here were provided through ellipsometry and force-distance measurements (see Supporting Information).

2.4. Thermal Effects

In order to confirm PAT as the main mechanism occurring in the pc-M1IM2 nanorectenna, it is crucial to rule out any other effects that might be expected under illumination conditions. In particular, thermal effects such as thermal expansion, Seebeck effect, and thermal assisted photoemission due to temperature rise in the illuminated nanocone, might negatively influence the conduction outcome of the nanorectenna by partial or even complete suppression of the optical rectification.^[63] In this regard, the first clue about the limited presence of any thermal effect is provided by the reasoning that a structural expansion of the nanocone should occur upon a significant increase in temperature. This modification would especially affect the nanocone along its main axis, pushing the nanocone tip into

the IM2 substrate, possibly reducing the oxide thickness. By assuming a strong thermal effect due to the illumination conditions, the current should, over time, show an amplitude change over the whole considered bias range with a directionality related to the applied bias: positive in the first quadrant and negative in the third quadrant. This behavior is not observed in Figure 3a where a bias independent illuminated I - V characteristic is instead shown hence suggesting the limited, if not absent, thermal expansion effect on the measured current.

To further confirm these considerations, light-induced thermal effects in a nanocone are carefully addressed by performing numerical FEM-based simulations where Maxwell and heat diffusion equations were simultaneously solved.^[64] The results, illustrated in the Supporting Information, show that with the parameters employed in the experiment (light power, focal spot, polarization), a temperature rise of less than 2 K was achieved, making any thermal expansion and thermally assisted photoemission negligible. Finally, the presence of thermoelectric contributions through the Seebeck effect can also be neglected in our nanorectenna as these contributions were only reported in MIM samples characterized by linear I - V ,^[65] which is not the present case. These arguments confirm negligible thermal effects on the electric behavior of the nanorectenna, pointing to PAT as the primary working mechanism.

Another possible mechanism that could in principle occur is related to the thermal-induced electro-chemistry modification of TiO_2 , in particular in creating oxygen vacancy filaments.^[66] However, Figure S3, Supporting Information, reveals an unchanged morphology for the three different maps performed over the same area with different amounts of force, inferring that no physical deformation/electroformation occurred in our samples. Small thickness, low working voltage range and negligible thermal changes (see Figure S6, Supporting Information)^[66] altogether eliminate the possibility of electroformation in our rectenna configuration. This is further confirmed by the absence of any memristive behavior,^[67] since our I - V measurements on multiple samples under identical conditions always returned a behavior without any memory effect/hysteresis.

2.5. Multi-Tip Nanorectenna

In order to investigate the scaling-up potential of the nanorectenna architecture, an array of tips (multi-tip) was fabricated on an AFM cantilever probe. In this regard, a square array of 3×3 tips was realized (Figure 5a,b) with a separation of 300 nm, hence with an area covering the entire focal spot region. This configuration was then tested to verify whether an enhanced photocurrent is retrieved with respect to the single nanorectenna. The resulting I - V characteristic obtained with a multi-tip nanorectenna on top of TiO_x/Ti -50 nm is shown in Figure 5c, which confirms the same optical rectification signature of a single nanorectenna. Importantly, the histograms of Figure 5d remarkably demonstrate that the zero-bias photocurrent generated with several nanocones is statistically larger than a single nanocone, therefore supporting that an actual nanorectenna device could indeed result from the integration of many nanocones on the same chip.^[68,69]

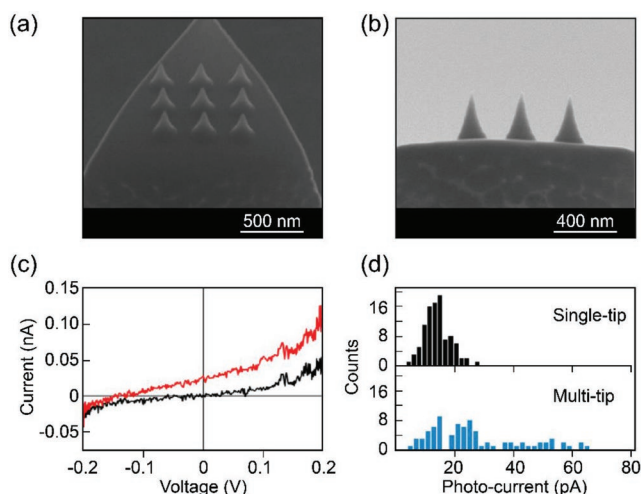


Figure 5. Experimental results with multi-tip nanorectenna. a) Top view in electron micrograph of multi-tip scanning probe, b) side view. c) I - V characteristics performed with multi-tip nanorectenna in both dark (black color) and illuminated (red color) conditions. d) Histograms of short-circuit currents recorded with single tip probe (black histogram) and multi-tip probe (blue histogram). In all cases a TiOx/Ti-50 nm/quartz substrate was employed.

However, a multi-tip probe of this kind introduces some experimental challenges, as all the tips need to be in controlled contact with the underneath substrate for best operation conditions. SEM images found that the fabricated tips have indeed ± 5 nm differences in height, which was also sensed by the AFM feedback system during electrical measurements. This fabrication limitation, together with the tilting of the cantilever, suggests that different approaches should be taken into consideration for the fabrication of nanorectenna integrated chips, where a geometrically static device would likely operate with better performance.^[70] Regardless of the actual final geometrical configuration, these measurements indicate that under the assumption of proper electrical connection between the tips and the underneath material, if all the tips undergo the same kind of optical excitation, the resulting overall photocurrent should scale up linearly with the number of tips.

2.6. Efficiency

One of the most important quantities for evaluating the performance of an energy conversion device is its efficiency, here linked with the capability to convert electromagnetic energy into collectable current. In this regard, the quantities which have to be taken into account to assess the efficiency are the open-circuit voltage V_{OC} and the short-circuit current I_{SC} , whose product provides the theoretical power P_T , similarly to photovoltaic solar cells. Specifically, for the nanorectenna device, these values are expected to be read in the second quadrant of the I - V characteristic, as shown in Figure 3a, and in agreement with the PAT theory (differently from semiconductor solar cells which operate in the fourth quadrant). An estimate of the nanorectenna maximum efficiency η can then be calculated as

$$\eta = \frac{P_{out,max}}{P_{in}} = \frac{FF \cdot P_T}{P_{in}} = \frac{FF \cdot I_{SC} \cdot V_{OC}}{P_{in}} \quad (2)$$

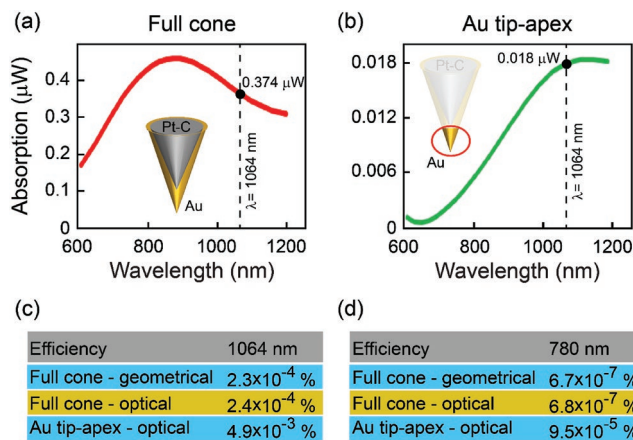


Figure 6. a,b) Calculated absorption when an input intensity of 12.95 MW m^{-2} impinges on the cone sample with a polarization angle of 12° with respect to the X -axis (see Figure 1a). The dashed lines are located at 1064 nm where they highlight the absorption value. All the calculations consider a cone formed by Pt-C, with base diameter of 200 nm, height 300 nm, and apex radius 10.5 nm, as from experimental data. Furthermore, an Au layer of 20 nm deposited from the apex side is considered, thus to mimic the fabricated structure. The cone apex contacts, with a 1.3 nm contact radius (see Supporting Information), a 2 nm thick TiOx layer on top of a 50 nm Ti film. a) The full cone has been considered, both the Pt-C core and the Au coating. b) Only the 20 nm of gold forming the tip-apex right above the TiOx substrate has been considered. c) Efficiency at $\lambda = 1064 \text{ nm}$ (input intensity 12.95 MW m^{-2}) and d) at $\lambda = 780 \text{ nm}$ (input intensity 7.10 MW m^{-2}) calculated for three scenarios differentiating one another by the portion of cone considered for the calculation. From top to bottom: (Full cone—geometrical) Geometrical cross section of the entire cone; (Full cone—optical) Absorption cross section of the entire cone; (Au tip-apex—optical) Absorption cross section of the Au tip-apex (20 nm thick coating).

where FF is the fill factor and P_{in} is the geometrical or optical absorbed power. In this respect, the tables in Figure 6c,d show three different efficiencies obtained for both $\lambda = 1064 \text{ nm}$ and $\lambda = 780 \text{ nm}$, respectively.

In particular, the full cone—geometrical efficiency aims at a straight comparison to the works of Sharma et al. and Anderson et al.,^[22–24] which report the best to date efficiencies of $\approx 10^{-6} \%$ (for $\lambda = 532, 638, \text{ and } 1064 \text{ nm}$). Our configuration provides an improved efficiency $2.3 \times 10^{-4} \%$ at $\lambda = 1064 \text{ nm}$ and $FF = 0.25$ (as resulting from the triangle shape of Figure 3a). This value was calculated for the experimental values $I_{SC,1064nm} = 23.5 \text{ pA}$ and $V_{OC,1064nm} = 151.5 \text{ mV}$ obtained under an input intensity of 12.95 MW m^{-2} (see Figure 3a) and considering a geometrical absorption based on the effective area corresponding to the 2D projection of a cone of height 300 nm, base diameter 200 nm and apex-deposited Au layer of 20 nm, as depicted in Figure 2d (for $\lambda = 780 \text{ nm}$ refer to Supporting Information). Even though this result is an important step forward in efficiency, it should be stressed that these values are still far away from representing devices with actual practical applications.

We went then further in our analysis by considering two additional scenarios associated with more realistic situations. Here, instead of considering a geometrical absorption of the incident radiation impinging on the Au nanocone, the optical absorption spectra were employed as depicted in Figure 6a,b. In particular: i) Full cone—optical, with $P_{in} = 0.37 \mu\text{W}$ at 1064 nm, results from the absorption cross-section of the entire cone,

including the Pt-C core and the Au coating (20 nm coating). Interestingly, in this case the absorption cross section results to be slightly higher than the geometrical one, hence the small improvement in the efficiency; ii) Au tip-apex—optical, with $P_{\text{in}} = 0.018 \mu\text{W}$ at 1064 nm, only considers the portion of the cone with dimensions inside the $e\text{MFP}$ (only the top 20 nm of Au), hence containing the HEs which may move from the cone antenna into the Ti substrate through the TiO_x layer. Under this assumption, a remarkable efficiency of $4.9 \times 10^{-3} \%$ is achieved. Importantly, the comparison between the data in Figure 6c,d highlights the importance of the resonant condition, as it can strongly contribute to a performance improvement. This suggests that adopting a combination of resonant asymmetric geometries could represent a viable path for achieving high-performance rectennas at high-frequencies.

3. Conclusion

A plasmonic rectenna has been designed and tested for high-frequency rectification. The rectenna consists of a conical Au antenna capturing the electromagnetic radiation and is coupled to a TiO_x/Ti insulator-metal substrate through its tip-apex, all together forming an AC rectifier. The rectifying system, extending the general scheme of a MIM junction to a plasmonic MIM junction, shows important asymmetric characteristics, which guarantee one-directional DC current flux, from the cone to the substrate. Three types of asymmetries are exploited: i) geometrical, owing to the different morphology between the antenna (conical) and substrate (planar), determining on the former element an improved interaction with the electromagnetic radiation, ii) material, as metals with different work functions have been employed for realizing the plasmonic MIM junction (antenna Au and substrate Ti), and iii) phenomenological, indeed while the Au cone can emit electrons through surface electron scattering owing to its nano dimension, in comparison the Ti substrate undergoes a very limited electron emission process, due to its flat morphology. Theoretically and numerically, the conical antenna has been designed for resonating at 1064 nm, yet with the capability to provide light-harvesting also at higher frequencies. Thermal simulations have also ruled out any possible influence on the measured current due to temperature fluctuations. Experimentally, the system was fabricated via top-down techniques and characterized to retrieve the I - V characteristic. The results, consistent with photon assisted theory analysis, demonstrated an overall efficiency about two orders of magnitude higher than the state-of-the-art in the high-frequency range. In order to provide a robust reading of the optoelectrical response of the plasmonic rectenna, an AFM system was adopted to scan the Au cone over the TiO_x/Ti substrate. This procedure allowed for a detailed study of the role played by the substrate, by analyzing the friction upon the application of different contact forces. Furthermore, envisioning larger-scale applications to address realistic needs, we also demonstrated the possibility of integrating several different rectennas with consistent performance, thereby providing a scalability route. Indeed, fabrication techniques such as imprinting lithography would allow large rectenna chips, beyond the prototypical examples shown in this work. Overall,

our results show an efficiency improvement of at least two orders of magnitudes with respect to the best reported high-frequency result to date. Still, importantly, our work suggests that through a proper device engineering (e.g., matching between wavelength and antenna geometry or adoption of multi-resonant rectennas), it is possible to improve the efficiency further, possibly reaching values appealing for commercial light-harvesting rectifying devices. In this respect, it is stressed the need for an analytical/numerical predictive tool capable of providing the rectenna I - V characteristic even in the visible range. A tool of this kind would be beneficial for understanding and engineering high frequency rectenna operation.

4. Experimental Section

Numerical Simulations: The Pt-C core nanocone top-coated with ≈ 20 nm of Au and in contact with a TiO_x/Ti substrate was simulated with 3D electromagnetic FEM simulation software Comsol Multiphysics. As design parameters were considered the diameter of the nanocone base, its height, the nanocone apex diameter, and thickness of the Au layer together with the thickness and materials forming the underneath layer. A linearly polarized light with a polarization angle of 12° with respect to the X-axis (mimicking the experimental arrangement) was assumed as excitation source, as shown in Figure 1a. The refractive of TiO_x was taken equal to 2.3 (similar to the ellipsometry data), the refractive index of Ti was implemented by adopting a Drude-Lorentz formalism as in Rakic et al.,^[71] while Au was taken from Alabastri et al.^[72]

Fabrication of the pc-M1IM2 Nanorectenna: The nanocone antenna, as resulting from the numerical simulations, was fabricated using FIB milling (FEI Nanolab 600 dual beam) with Ga ion beam. A contact mode silicon AFM cantilever probe (MikroMasch CSC38-Al) with a long cone/pyramid was chosen as platform for the nanocone fabrication (lever length 350 μm , lever thickness 1 μm , and probe height 15 μm). In particular, the Si cantilever probe was coated with a 7 nm Ti layer to increase its adhesion capability followed by a further coating of 15 nm of Au to create a uniform conductive layer. Afterward, the AFM tip was etched creating a plateau where a Pt-C nanocone was grown via GIS system. Importantly, this approach could guarantee the realization of a Pt-C nanocone with a ≈ 10 nm apex radius with an extremely high reproducibility. An over-layer of ≈ 20 nm of Au, thick enough to support SPPs, was then deposited via Ar ion sputter on the structure followed by 20 min of annealing process at 195 $^\circ\text{C}$ characterized by a fast heating ramp and a slowly decaying cooling ramp. This final procedure was set in order to smooth as much as possible the nanocone surface, necessary condition for improved electric contact with the underneath substrate.

The nature of the nanorectenna assembly and characterization procedure requires a reduced surface roughness for the IM2 substrate, as it could minimize the variability in the rectified current yield. Due to this necessity and considering that the substrate morphology strongly influences the roughness of the coating materials, quartz with a surface roughness of 0.6 nm was used as substrate material. In particular, the quartz was first cleaned with Piranha solution, then with acetone, followed by iso-propanol. Afterward, the clean quartz substrate was dried with nitrogen, washed again with a piranha solution, and finally dried with nitrogen once again. Immediately after the conclusion of this procedure, 50 nm of Ti were deposited on top of the quartz with an electron beam evaporator (Kurt J. Lesker Company PVD 75) adopting a deposition rate as slow as 0.02 nm s^{-1} , a rate chosen to minimize the surface roughness. Afterward, the growth of the native TiO_x through the surface oxidation of Ti was induced by inserting the sample inside an ISO 6 cleanroom at room temperature for ≈ 1 h before characterization measurements.

The Optical System: A commercial AFM (Veeco AFM-Multimode V) was utilized as core component of the optical and electronic systems. The AFM was used in contact mode to perform conducting atomic force spectroscopy of the IM2 nanorectenna component. The main advantage

of this setup was the free positioning of the Au nanocone which can be brought in contact with the IM2 layer in a controlled manner while protecting the nano-antenna from shape deformation.

The Au nanocone was illuminated through the side entrance of the AFM stage. The angle of incidence of the laser light was 12° with respect to the X-axis, see Figure 1a. In this regard, a beam expander was used to expand the beam to fill the wide entrance aperture of the bright and dark field objective (BD Plan Apo SL20X) to obtain a NA of 0.28, so to minimize the focal spot down to a diameter of $4\ \mu\text{m}$ (at 1064 nm). A ring of several white LEDs was also positioned right in front of the BD objective with the purpose to illuminate the AFM chamber and simultaneously to collect the scattered light for live imaging through a Thorlabs CCD USB camera. Furthermore, a transparent window was placed along the main optical path and immediately before the focal spot to partially reflect light toward a fast photo-diode having the function to continuously monitor the power of the laser beam throughout the experiment. Finally, the excitation laser beam (single mode IPG-Fiber laser) was polarized along the axis of the cone (Z-axis) with a set of polarizers and half wave plates.

Electronic Instrumentation System: A function generator was used to apply DC or low frequency AC bias to the sample. The bias was applied to the bottom electrode (M2). The nanocone was instead the grounding top electrode virtually grounded by the inverting terminal of the Trans-Impedance Amplifier (TIA, FEMTO-50K, see Supporting Information) which was employed to amplify the currents generated across the MIM junction into voltages with a gain of $10^8\ \text{V A}^{-1}$ over a large bandwidth of 50 kHz. The tunneling currents detected in the single pc-MIM junctions were typically in the range from pA to few nA, therefore particular care has been taken to adopt solutions minimizing the noise in the current measurements. In particular, the noise was decreased by employing shielded and short cables prior to the amplification stage, shielding wires, and by connecting all instruments to a common ground (optical bench) through the use of electronics filters after the amplification of the current to voltage. In order to avoid any noise amplification, the TIA was kept very close to the AFM probe. Furthermore, an analogic filter (SIM965 Stanford Research Systems, settings in Supporting Information) was employed to clean the TIA signal from frequencies above 10 kHz such as the 40 kHz signal originating from the electromagnetic coupling with the AC switching power lines of instruments. The output of the TIA as well as the applied bias voltage, laser power measured by the photo-diode, the deflection signal output of the AFM due to the contact between the Au nanocone and the TiO_2/Ti substrate were acquired with a fast National Instruments 8-channel data acquisition (DAQ) device. An optical chopper was used to modulate the laser beam at 371 Hz, hence far from both the low frequency acoustic noise and the AC power lines 60 Hz frequency. Finally, when fast laser modulation was employed, a lock-in amplifier (Stanford Research Systems SR830) was used for in-phase measurements.

Supporting Information

Supporting Information is available from the Wiley Online Library or from the author.

Acknowledgements

R.M. and J.C. have contributed equally to this work. R.P.Z. would like to acknowledge the support from the NSFC project, grant no. 32071317. R.P.Z. and A.A. wish to thank the support from the European Space Agency, ARIADNA grant. A.A. acknowledges support from the National Science Foundation under Grant No. IIP-1941227. D.G. acknowledges support from the H2020 FET-Open Program Grant No. 964995 "DNAFAIRYLIGHTS".

Open access Funding provided by Istituto Italiano di Tecnologia within the CRUI-CARE Agreement.

Conflict of Interest

The authors declare no conflict of interest.

Data Availability Statement

The data that support the findings of this study are available from the corresponding author upon reasonable request.

Keywords

energy harvesting, metal-insulator-metal diodes, optical rectifiers, plasmonic diodes

Received: December 2, 2021

Revised: February 12, 2022

Published online:

- [1] W. C. Brown, *IEEE Trans. Microwave Theory Tech.* **1984**, *32*, 1230.
- [2] R. L. Bailey, *J. Eng. Power* **1972**, *94*, 73.
- [3] S. Faris, T. Gustafson, J. Wiesner, *IEEE J. Quantum Electron.* **1973**, *9*, 737.
- [4] M. Heiblum, S. Wang, J. Whinnery, T. Gustafson, *IEEE J. Quantum Electron.* **1978**, *14*, 159.
- [5] G. M. Elchinger, A. Sanchez, C. F. Davis Jr, A. Javan, *J. Appl. Phys.* **1976**, *47*, 591.
- [6] J. Kern, R. Kulloock, J. C. Prangasma, M. Emmerling, M. Kamp, B. Hecht, *Nat. Photonics* **2015**, *9*, 582.
- [7] N. M. Miskovsky, P. H. Cutler, A. Mayer, B. L. Weiss, B. Willis, T. E. Sullivan, P. B. Lerner, *J. Nanotechnol.* **2012**, *2012*, 512379.
- [8] E. Donchev, J. S. Pang, P. M. Gammon, A. Centeno, F. Xie, P. K. Petrov, J. D. Breeze, M. P. ryan, D. J. Riley, N. McN Alford, *MRS Energy Sustainability* **2014**, *1*, E5.
- [9] C. A. Reynaud, D. Duch, J.-J. Simon, E. Sanchez-Adaime, O. Margeat, J. Ackermann, V. Jangid, C. Lebouin, D. Brunel, F. Dumur, D. Gignes, G. Berginc, C. A. NijhuiS, L. Escoubas, *Prog. Quantum Electron.* **2020**, *72*, 100265.
- [10] M. Shanawani, D. Masotti, A. Costanzo, *Electronics* **2017**, *6*, 99.
- [11] S. J. Byrnes, R. Blanchard, F. Capasso, *Proc. Natl. Acad. Sci. U. S. A.* **2014**, *111*, 3927.
- [12] S. Joshi, G. Moddel, *J. Appl. Phys.* **2015**, *118*, 084503.
- [13] J. A. Bean, A. Weeks, G. D. Boreman, *IEEE J. Quantum Electron.* **2011**, *47*, 126.
- [14] M. N. Gadalla, M. Abdel-Rahman, A. Shamim, *Sci. Rep.* **2014**, *4*, 4270.
- [15] P. S. Davids, R. L. Jarecki, A. Starbuck, D. B. Burckel, E. A. Kadlec, T. Ribaudo, E. A. Shaner, D. W. Peters, *Nat. Nanotechnol.* **2015**, *10*, 1033.
- [16] W. Amara, A. Yahyaoui, N. Eltresy, M. Aseeri, B. Hakim, Y. Al-Turki, H. Rmili, *Int. J. Numer. Model.* **2020**, *34*, e2836.
- [17] P. S. Davids, J. Kirsch, A. Starbuck, R. Jarecki, S. D. Peters, *Science* **2020**, *367*, 1341.
- [18] A. Weerakkody, A. Belkadi, G. Moddel, A. C. S. Appl, *Nano Mater.* **2021**, *4*, 2470.
- [19] A. Belkadi, A. Weerakkody, G. Moddel, *Nat. Commun.* **2021**, *12*, 2925.
- [20] M. Dragoman, M. Aldrigo, *Appl. Phys. Lett.* **2016**, *109*, 113105.
- [21] A. Hemmetter, X. Yang, Z. Wang, M. Otto, B. Uzlu, M. Andree, U. Pfeiffer, A. Vorobiev, J. Stake, M. C. Lemme, D. Neumaier, *ACS Appl. Electron. Mater.* **2021**, *3*, 3747.
- [22] A. Sharma, V. Singh, T. L. Bougher, B. A. Cola, *Nat. Nanotechnol.* **2015**, *10*, 1027.

- [23] E. C. Anderson, T. L. Bougher, B. A. Cola, *Adv. Electron. Mater.* **2018**, 4, 1700446.
- [24] E. C. Anderson, B. A. Cola, *ACS Appl. Electron. Mater.* **2019**, 1, 692.
- [25] A. V. Bragas, S. M. Landi, O. E. Martinez, *Appl. Phys. Lett.* **1998**, 72, 2075.
- [26] P. Periasamy, H. L. Guthrey, A. I. Abdulagatov, P. F. Ndione, J. J. Berry, D. S. Ginley, S. M. George, P. A. Parilla, R. P. O'Hayre, *Adv. Mater.* **2013**, 25, 1301.
- [27] A. Mayer, M. S. Chung, P. B. Lerner, B. L. Weiss, N. M. Miskovsky, P. H. Cutler, *J. Vac. Sci. Technol. B* **2011**, 29, 041802.
- [28] A. Mayer, M. S. Chung, B. L. Weiss, N. M. Miskovsky, P. H. Cutler, *Nanotechnology* **2010**, 145204.
- [29] K. Choi, G. Ryu, F. Yesilkoy, A. Chryssis, N. Goldsman, M. Dagenais, M. Peckerar, *J. Vac. Sci. Technol., B: Microelectron. Nanometer Struct.–Process., Meas., Phenom.* **2010**, 28, C6050.
- [30] G. Moddel, A. Weerakkody, D. Doroski, D. Bartusiak, *Symmetry* **2021**, 13, 517.
- [31] K. M. Evenson, M. Inguscio, D. A. Jennings, *J. Appl. Phys.* **1985**, 57, 956.
- [32] G. Jayaswal, A. Belkadi, A. Meredov, B. Pelz, G. Moddel, A. Shamim, *Mater. Today Energy* **2018**, 7, 1.
- [33] E. H. Hauge, J. A. Støvneng, *Rev. Mod. Phys.* **1989**, 61, 917.
- [34] M. Razavy, *Quantum Theory of Tunnelling*, World Scientific, Canada **2013**.
- [35] G. Moddel, S. Grover, *Rectenna Solar Cells*, Springer, New York **2013**.
- [36] V. L. Dalal, *J. Appl. Phys.* **1971**, 42, 2274.
- [37] Y. Nishijima, S. Morimoto, A. Balçytis, T. Hashizume, R. Matsubara, A. Kubono, N. To, M. Ryu, J. Morikawac, S. Juodkakis, *J. Mater. Chem. C* **2022**, 10, 451.
- [38] H. Wang, A. Toma, H. Y. Wang, A. Bozzola, E. Miele, A. Haddadpour, G. Veronis, F. De Angelis, L. Wang, Q. D. Chen, H. L. Xu, H. B. Sun, R. P. Zaccaria, *Nanoscale* **2016**, 8, 13445.
- [39] H. Wang, H. Y. Wang, A. Bozzola, A. Toma, S. Panaro, W. Raja, A. Alabastri, L. Wang, Q. D. Chen, H. L. Xu, F. De Angelis, H. B. Sun, R. P. Zaccaria, *Adv. Funct. Mater.* **2016**, 26, 6198.
- [40] R. Proietti Zaccaria, A. Alabastri, F. De Angelis, G. Das, C. Liberale, A. Toma, A. Giugni, L. Razzari, M. Malerba, H. Bo Sun, E. Di Fabrizio, *Phys. Rev. B* **2012**, 86, 35410.
- [41] A. O. Govorov, H. Zhang, H. V. Demir, Y. K. Gun'kode, *Nanotoday* **2014**, 9, 85.
- [42] L. V. Besteiro, X. T. Kong, Z. Wang, G. Hartland, A. O. Govorov, *ACS Photonics* **2017**, 4, 2759.
- [43] A. Giugni, B. Torre, A. Toma, M. Francardi, M. Malerba, A. Alabastri, R. Proietti Zaccaria, M. I. Stockman, E. Di Fabrizio, *Nat. Nanotechnol.* **2013**, 8, 845.
- [44] U. Kreibitz, *J. Phys. F: Met. Phys.* **1974**, 4, 999.
- [45] L. V. Besteiro, A. O. Govorov, *J. Phys. Chem. C* **2016**, 120, 19329.
- [46] C. Donolato, *J. Appl. Phys.* **2004**, 95, 2184.
- [47] G. D. J. Smit, S. Rogge, T. M. Klapwijk, *Appl. Phys. Lett.* **2002**, 81, 3852.
- [48] S. Tuccio, L. Razzari, A. Alabastri, A. Toma, C. Liberale, F. De Angelis, P. Candeloro, G. Das, A. Giugni, E. Di Fabrizio, R. Proietti Zaccaria, *Opt. Lett.* **2014**, 39, 571.
- [49] H. Nguyen, P. Cutler, T. E. Feuchtwang, Z.-H. Huang, Y. Kuk, P. Silverman, A. Lucas, T. E. Sullivan, *IEEE Trans. Electron Devices* **1989**, 36, 2671.
- [50] S. V. Boriskina, J. Zhou, Z. Ding, G. Chen, *Photonics* **2018**, 5, 4.
- [51] A. Urban, *Optothermal Manipulation of Phospholipid Membranes with Gold Nanoparticles*, Cuvillier Verlag, Inhaberin Annette Jentzsch-Cuvillier, Göttingen **2011**.
- [52] A. Stolz, J. Berthelot, M. M. Mennemanteuil, G. L. Markey, V. Meunier, A. Bouhelier, *Nano Lett.* **2014**, 14, 2330.
- [53] S. Grover, S. Joshi, G. Moddel, *J. Phys. D: Appl. Phys.* **2013**, 46, 135106.
- [54] D. R. Ward, F. Hüser, F. Pauly, J. C. Cuevas, D. Natelson, *Nat. Nanotechnol.* **2010**, 5, 732.
- [55] P. S. Davids, J. Shank, *Phys. Rev. B* **2018**, 97, 075411.
- [56] P. Tien, J. Gordon, *Phys. Rev.* **1963**, 129, 647.
- [57] J. R. Tucker, M. J. Feldman, *Rev. Mod. Phys.* **1985**, 57, 1055.
- [58] G. Platero, R. Aguado, *Phys. Rep.* **2004**, 395, 1.
- [59] J. M. Beebe, B. Kim, J. W. Gadzuk, C. D. Frisbie, J. G. Kushmerick, *Phys. Rev. Lett.* **2006**, 97, 026801.
- [60] J. G. Simmons, *J. Appl. Phys.* **1963**, 34, 1793.
- [61] U. Celano, T. Hantsche, G. Giammaria, R. C. Chintala, T. Conard, H. Bender, W. Vandervorst, *J. Appl. Phys.* **2015**, 117, 214305.
- [62] J. J. Åkerman, R. Escudero, C. Leighton, S. Kim, D. A. Rabson, R. W. Dave, J. M. Slaughter, I. K. Schuller, *J. Magn. Magn. Mater.* **2002**, 240, 86.
- [63] M. M. Mennemanteuil, G. Colas-des-Francis, M. Buret, A. Dasgupta, A. Cuadrado, J. Alda, A. Bouhelier, *Nanophotonics* **2018**, 7, 1917.
- [64] J. Cunha, T. L. Guo, G. Della Valle, A. N. Koya, R. Proietti Zaccaria, A. Alabastri, *Adv. Opt. Mater.* **2020**, 8, 2001225.
- [65] M. Bareiß, P. M. Krenz, G. P. Szakmany, B. N. Tiwari, D. Kalblein, A. O. Orlov, G. H. Bernstein, G. Scarpa, B. Fabel, U. Zschieschang, H. Klauk, W. Porod, P. Lugli, *IEEE Trans. Nanotechnol.* **2013**, 12, 1144.
- [66] J. J. Yang, F. Miao, M. D. Pickett, D. A. A. Ohlberg, D. R. Stewart, C. N. Lau, R. S. Williams, *Nanotechnology* **2009**, 20, 215201.
- [67] J. J. Yang, M. D. Pickett, X. Li, D. A. A. Ohlberg, D. R. Stewart, R. S. Williams, *Nat. Nanotechnol.* **2008**, 3, 429.
- [68] M. Alexe, D. Hesse, *Nat. Commun.* **2011**, 2, 256.
- [69] J. E. Spanier, V. M. Fridkin, A. M. Rappe, A. R. Akbashev, A. Polemi, Y. Qi, Z. Gu, S. M. Young, C. J. Hawley, D. Imbrenda, G. Xiao, A. L. Bennet-Jackson, C. L. Johnson, *Nat. Photonics* **2016**, 10, 611.
- [70] P. B. Lerner, P. H. Cutler, N. M. Miskovsky, *J. Nanophotonics* **2015**, 9, 093044.
- [71] A. D. Rakić, A. B. Djurišić, J. M. Elazar, M. L. Majewski, *Appl. Opt.* **1998**, 37, 52710.
- [72] A. Alabastri, S. Tuccio, A. Giugni, A. Toma, C. Liberale, G. Das, F. De Angelis, E. di Fabrizio, R. Proietti Zaccaria, *Materials* **2013**, 6, 4879.